Rapid Detection of Co-Seismic Ionospheric Disturbances Associated With the 2015 Illapel, the 2014 Iquique and the 2011 Sanriku-Oki Earthquakes

S. Sanchez, E. Kherani, E. Astafyeva, E. de Paula

Rapid detection of co-seismic ionospheric disturbances associated with the 2015 Illapel, the 2014 Iquique and the 2011 Sanriku-Oki earthquakes

S. A. Sanchez[1*], E. A. Kherani[1], E. Astafyeva[2] and E. R. de Paula[1]

[1]Instituto Nacional de Pesquisas Espaciais, São José dos Campos, 1222 7010, Brazil
[2]Université Paris Cité, Institut de Physique du Globe de Paris, CNRS UMR 7154, Paris, France

Key Points:

- A new methodology to rapidly estimate the time and the altitude of detection of co-seismic ionospheric disturbances (CID),
- The methodology uses data from near-epicenter seismic stations to calculate the seismic peak time as an alternative to the earthquake onset,
- First report on detection of CID as soon as 400 seconds after the earthquake onset and 250-430 seconds after the seismic peak time,

*INPE, Av. dos Astronautas 1758, 12227-010 São José dos Campos, Brazil

Corresponding author: S.A. Sanchez, saul.juarez@inpe.br, saulsjf@gmail.com

Abstract

Co-seismic Ionospheric disturbances (CID, or "ionoquakes") are disturbances in the electron density or total electron content (TEC) of the ionosphere, produced by the ground motion due to earthquakes. Usually, ionoquakes are detected in the near-epicentral region within 8-10 minutes after an earthquake onset time. In this work, we present a new methodology that allows to estimate the CID arrival time based on determining the CID peak time in TEC measurements with respect to the peak time of seismic waves registered by the nearest seismic station. Our methodology also allows to understand the altitude of GNSS detection that otherwise remains ambiguous. We apply the newly developed techniques to detect CID signatures associated with three large earthquakes: the 2015 Illapel, the 2014 Iquique, and the 2011 Sanriku-Oki. We show that for these events, the CID arrive 250-430 seconds after the time of the seismic wave peak, or 350-700 s after the earthquake onset time. Our analysis show that the first CID are detected at the altitudes of 150-180 km (the Sanriku earthquake) and of 200-300 km (the Illapel and the Iquique earthquakes). The disturbances represent high-frequency acoustic oscillations that propagate with a horizontal speed faster than 0.75 km/s.

1 Introduction

It is known that large earthquakes can generate acoustic and gravity waves that further produce disturbances in the ionosphere (Calais & Minster, 1995; Heki & Ping, 2005; Liu et al., 2006; Lognonné, 2009; Astafyeva et al., 2009; Chum et al., 2012; Occhipinti et al., 2013; Afraimovich, E. L. et al., 2013; Cahyadi & Heki, 2015; Thomas et al., 2018; Astafyeva & Shults, 2019; Sanchez et al., 2022; Bravo et al., 2022). Such disturbances are referred to as Coseismic Ionospheric Disturbances (CIDs) or ionoquakes. They usually propagate at horizontal speeds between 600 m/s and 3 km/s (Astafyeva et al., 2009; Rolland et al., 2011; Astafyeva et al., 2014), and their oscillation frequency lies in the range 1-10 mHz (Bagiya et al., 2019; Manta et al., 2020; Sanchez et al., 2022).

The CIDs propagating at the acoustic wave speed (i.e., 600-1000 m/s) are usually detected in the near-epicentral area only 8-10 min after an earthquake (Heki & Ping, 2005; Kherani et al., 2012; Cahyadi & Heki, 2015; Thomas et al., 2018; Astafyeva & Shults, 2019). Such a short timing opens a possibility of use CIDs to enhance the capability of early tsunami warning by using ionospheric data Occhipinti (2015); Astafyeva (2019, 2020).

In recent years, a few studies have reported early and rapid detection of CIDs, i.e. less than the "nominal" 480-600 seconds after an earthquake. For instance, the first CIDs due to the 2011 Tohoku-oki earthquake were detected as early as 420-464 seconds after the earthquake onset time Astafyeva et al. (2011, 2013); Bagiya et al. (2020); Chum et al. (2016). Early CID arrivals (440-480 sec) have also been reported for the Mw7.4 March 9, 2011 Sanriku-oki earthquake in Japan Thomas et al. (2018); Astafyeva and Shults (2019). The phenomenon of early CID arrivals is not well understood yet. In the case of the Tohoku-oki earthquake, they were explained by the generation of large shock-waves Astafyeva et al. (2011), and/or by low LOS elevation angles Astafyeva et al. (2013).

In this work, we present a new methodology allowing to 1) rapidly detect CID in total electron content (TEC) data times series and to estimate the CID arrival time; 2) estimate the altitude of ionospheric detection. We further apply this technique to analyze co-seismic ionospheric signatures due to the Mw8.3 Illapel earthquake of September 16, 2015, the Mw8.2 Iquique earthquake of April 01, 2014, and the Mw7.3 Sanriku-oki earthquake of March 09, 2011.

2 Earthquake events and Seismic and TEC Data

The Illapel and Iquique earthquakes of Mw8.3 and 8.2 respectively were triggered near the Chile subduction zone, in South America. Seismicity in the Chilean region is defined by the subduction of the oceanic Nazca plate under the South American plate. This subduction zone is well known for harboring large EQs (Carrasco et al., 2019). The Illapel earthquake occurred on September 16, 2015, at 22:54:32 UT. According to the U.S. Geological Survey (USGS), this earthquake was generated by thrust faulting, with the epicenter located at latitude = 31.57°S and longitude = 71.67°W, at a depth of 22.4 km (`https://earthquake.usgs.gov/earthquakes/eventpage/us20003k7a/technical`). The Iquique earthquake occurred on April 01, 2014, at 23:46:47 UT as a result of thrust faulting, with the epicenter located at latitude = 19.61°S and longitude = 70.77°W, at a depth of 25.5 km, (`https://earthquake.usgs.gov/earthquakes/eventpage/us20003k7a/technical`). The Sanriku-Oki earthquake of Mw7.4, occurred on March 9, 2011 at 02:45:20 UT at a depth of 32 km, with an epicenter at 38.435°N, 142.842°E (`https://earthquake.usgs.gov/earthquakes/eventpage/usp000hvhj/executive`).

Figure 1 illustrates the epicentral location and the shake map of the peak ground velocity for the Illapel, Iquique, and Sanriku-Oki earthquakes (source: `https://earthquake.usgs.gov/earthquakes`). The present study employs the seismic data derived from seismometers and TEC data derived from GNSS receivers. Figure 1 also illustrates the locations of seismic stations and GNSS receivers for the three earthquake events.

2.1 vTEC estimation from GNSS receivers

For Illapel and Iquique earthquakes, we examine the TEC data with 15 seconds sampling rate, retrieved from GNSS receivers of the permanent ground-based network UNAVCO (`http://www.unavco.org`) and CSN (`http://gps.csn.uchile.cl/`). For the analysis of the Sanriku-Oki earthquake, the original TEC data is with a 1-second sampling rate, retrieved from the GNSS Earth Observation Network System (GEONET). However, we lower the sampling rate from 1 second to 15 seconds in order to have identical data cadences for all events.

During the earthquakes, multiple GNSS satellites were visible by ground-based GNSS receivers. However, here we focus on PRNs = 12 and 24 for the Illapel earthquake, PRNs = 01, 20, and 23 for the Iquique earthquake, and PRN = 07 for the Sanriku-Oki earthquake. We have selected these PRNs since their projected locations at the ionospheric heights i.e., the Sub-Ionospheric Points (SIP) are within ∼450 km of the epicentral distance, and the elevation angle is more than 42°, except for the Sanriku-Oki earthquake, where the elevation angle was ∼ 30°.

The slant TEC (sTEC) and vertical TEC (vTEC) are estimated by using the phase and code measurements from ground-based GNSS-receivers (Hofmann-Wellenhof et al., 2008), based on Equation 1,

$$\mathrm{s}TEC = \frac{1}{40.308}\frac{f_1^2 f_2^2}{f_1^2 - f_2^2}(L_1\lambda_1 - L_2\lambda_2 + const + nL), \tag{1}$$

where f_1=1575.42 MHz and f_2=1227.60 MHz are the carrier-wave frequencies, $\lambda_1 = c/f_1$ and $\lambda_2 = c/f_2$ are the corresponding wavelengths in meters, c is the speed of light, L_1 and L_2 are the carrier phases, *const* is the unknown initial phase ambiguity, and nL is the error in determining the phase path. The TEC is measured in TEC units (TECU) with 1 TECU = $10^{16} el/m^2$. The exactitude of TEC estimation from phase measurements is about 0.01–0.02 TECU (Coster et al., 2013).

The vTEC is derived from sTEC using the following conversion Equation 2, (Klobuchar, 1987).

$$\mathrm{v}TEC = \mathrm{s}TEC.cos\left[arcsin\left(\frac{r_e}{r_e + H_{\mathrm{ION}}} cos\theta\right)\right], \tag{2}$$

where r_e is the Earth's radius, H_{ION} is the altitude of the ionospheric thin layer and θ is the satellite elevation angle.

2.2 V_{SISM} estimation from seismometers

To obtain the vertical velocity ($\mathrm{V_{SISM}}$) associated with the ground vibration from the seismometers, we employ the Python library: obspyDMT. ObspyDMT is an open-source toolbox for querying, retrieving, processing, and managing seismological data sets (Hosseini & Sigloch, 2017). The library downloads the data in count format, estimates the ground vibration, and minimizes the instrumental response contributions associated with the frequency response, amplifier, analog and digital filters, and digitization. We used a bandpass filter on the seismograms before deconvolution, with a tuple defining the four corner frequencies (0.02, 0.12, 10, 20) (Hosseini & Sigloch, 2017).

In the present study, $\mathrm{V_{SISM}}$ corresponds to the seismic station CO03 for the Illapel earthquake, PSGCX for the Iquique earthquake, and KSN for the Sanriku-Oki earthquake (Figure 1). To match the TEC sampling rate and to achieve identical spectral conditions between the two datasets, we reduce the seismic data sampling rate from 0.05 seconds to 15 seconds. The IRIS network (`http://ds.iris.edu/wilber3/find_event`) and National Research Institute for Earth Science and Disaster Resilience (NIED)-F-net (`https://www.fnet.bosai.go.jp/`) administer the seismic data.

3 Methodology

In contrast to previous studies that rely on the onset time of an earthquake, here we suggest to use the seismic peak time of the $\mathrm{V_{SISM}}$ for the estimation of the ionoquake detection time ($\mathrm{t_{detection}}$). The seismic peak time represents the time of the maximum seismic oscillations rather than the beginning time of the oscillations. We note, however, that the identification of the oscillation peak in the time series is comparatively unambiguous. The analysis subjects the $\mathrm{V_{SISM}}$ and TEC data to the spectral analysis procedure with identical spectral conditions, namely, the equal data length of 2 hours and a sampling rate of 15 seconds. Then, we examine the spectrogram in a frequency range of 0.13 mHz-33 mHz, and, for each frequency, we search for new oscillations in TEC starting from the corresponding peak onset time of $\mathrm{V_{SISM}}$ and in the vicinity of the epicenter.

We test two independent criteria to identify the peak time. In TEST-1, the peak time corresponds to the time of the first peak in the $\mathrm{V_{SISM}}$ and TEC oscillation. In TEST-2, the peak time corresponds to the time of the maximum in the $\mathrm{V_{SISM}}$ and TEC oscillations, i.e., corresponds to the time of the maximum amplitude. The peaks and the maxima are estimated by using the Python module "find-peaks". If the peak time of $\mathrm{V_{SISM}}$ and ionoquake are $\mathrm{t_{SISM}}$ and $\mathrm{t_{TEC}}$ respectively, then the ionoquake detection time can be defined as follows:

$$\mathrm{t_{detection}} = \mathrm{t_{TEC}} - \mathrm{t_{SISM}} \tag{3}$$

Since both $\mathrm{t_{SISM}}$ and $\mathrm{t_{TEC}}$ suffer identical time shift from spectral analysis, the ionoquake detection time $\mathrm{t_{detection}}$ remains unaffected by the time shift.

4 Results and Discussion

We first apply our methodology to the 2015 Illapel earthquake case. The time series of the seismic V_{SISM} and the ionospheric TEC data are shown in Figure 2. The seismic data are from the seismic station CO03, which is the closest to the epicenter, and TEC data corresponds to the SIP of Line-Of-Sight between the GPS station LSCH and G12 satellite (Figure 1). The SIP of the trajectory of PRN 12 passes over the seismic fault region and remains close to the epicenter (Figure 1). Figure 3 demonstrates the results of TEST-1 and TEST-2 in the left and right panels, respectively. We note the following characteristics:

- panels (A1, B1) reveal that the peak time of V_{SISM} depends on the frequency and occurs between 22:54 UT and 23:03 UT,
- panels (A2, B2) reveal that the peak time of ionoquakes also depends on the frequency,
- panels (A3, B3) reveal that the ionoquake detection time ranges between 250-550 seconds from the peak time of V_{SISM}, depending on the frequency and testing criteria,
- In both TEST-1 and TEST-2, the detection time of ionoquakes predominantly ranges between 250-400 seconds for the frequency range of 2-10 mHz,

Since both TEST-1 and TEST-2 confirm the ionoquake detection time range of 250-400 seconds, it can be considered as the valid ionoquake detection time in this frequency range, invariant of the criteria.

To validate the methodology of the detection time estimation, we apply it to the other SIP from various GPS stations within ±400 km CO03-SIP distance that detected ionoquakes, and we further examine the relationship between the detection time and the CO03-SIP distance. Figure 4(A, B) demonstrates the relationship for the frequency of 3.7 mHz and a frequency range of 3.2-10 mHz, respectively. We note the expected increase of the detection time with the distance. According to Figure 4(B), the minimum detection time is about 200 seconds at the distance of about -125 km, corresponding to the CO03-SIP distance of LSCH-G12. Since detection time prolongs symmetrically across the minimum ionoquake detection time location, the analysis identifies this detection as the "earliest ionoquake". Noticeably, it is located very close to the epicenter and fault region (denoted as red star and purple square in Figure 4). Therefore, our methodology not only estimates the detection time vs. distance characteristics but also, locates the earliest ionoquake close to the epicenter, based on the minimum detection time of the ionoquake.

In supplementary Figure S1, we present time snapshots of the TEC map during -300-1400 seconds where 0 seconds correspond to the peak onset time of V_{SISM} at the frequency of 3.7 mHz. We note that the TEC response becomes noticeable approximately 240-300 seconds after the earthquake onset, in confirmation of findings in Figures 3-4.

4.1 Possible subjectivities of the new methodology and their impacts on the ionoquake detection time

4.1.1 Seismic station Vs. Epicenter

Figure 4 shows the ionoquake detection time estimated with reference to a particular seismic station: CO03, instead of the epicenter location. In order to examine any possible subjectivity arising from the location of a seismic station, we carry out the ionoquake detection time estimation for various seismic stations (Figure S2). We note that the ionoquake detection time remains within 250-400 seconds near the epicenter, inde-

pendently on a choice of a seismic station. Therefore, the results of the present methodology are not subjective to a choice of seismic station.

4.2 Detection altitude for rapid ionoquakes

Figure 4(A, B) reveals the potential of the present methodology to identify the epicentral distance of the earliest ionoquake close to the epicenter. However, the location of CID/ionoquakes depends on the altitude (H_{ION}) of the thin ionospheric layer that is assumed to be H_{ION}= 300 km in Figure 4(A, B). Consequently, the horizontal distribution of ionoquakes will also depend on H_{ION}. To have an unambiguous ionoquake detection time, we examine the horizontal distribution of ionoquake detection time with varying H_{ION}=200, 250, 300, and 350 km (Figure 5). Interestingly, in Figure 5(C), for H_{ION}=300 km, the epicenter and the locations of minimum detection time are the closest. Therefore, the altitude region around 300 km is the most favorable altitude for the detection of the ionoquakes.

4.2.1 Onset time of an earthquake Vs. Peak onset time of V_{SISM}

In previous studies, the onset time of an earthquake was used as a reference for the seismic source time (Astafyeva et al., 2011, 2013; Astafyeva & Shults, 2019; Thomas et al., 2018). However, strictly speaking, the earthquake onset time does not represent the source time. The theory considers the co-seismic crustal uplift to be the source of CID. Consequently, it is the time of the co-seismic uplift that should be taken as the source time. However, seismic ruptures take time to propagate and cause crustal uplifts. For large earthquakes that are characterized by large-dimension faults, the delay between the earthquake onset and the maximum uplift can reach up to 3 minutes. For smaller events, the delay of 10 to 20 seconds is usually observed. While this time is the most correct to use, it cannot be calculated rapidly and without numerical modeling of seismic faults. Besides, different seismological and seismo-geodetic techniques provide different solutions.

Our approach suggests using the peak onset time of V_{SISM} that is calculated from seismic stations. The main advantage of our method is the independence on the seismological models, and also in the fact that it allows to calculate the CID arrivals very rapidly, i.e. potentially it can be used in near-real-time.

According to the USGS solutions, the Illapel earthquake onset time is 22:54:32 UT, and the maximum uplift occurred at 22:55:22 UT on the north-east from the epicenter. The peak onset time of V_{SISM} varies between 22:54 and 23:03 UT (Figure 3(A1, B1)), i.e., it is delayed between 32 seconds and 9 minutes from the USGS onset time, and 87 seconds to nearly 10 min from the seismic uplift time.

To examine the effects of the delay and other subjectivities arising from the usage of the seismic peak onset time rather than the earthquake onset time and the uplift time, we carry out the ionoquake detection time estimation with the following conventional definitions:

$$t1_{detection} = t_{TEC} - 22:54:32, \quad t2_{detection} = t_{TEC} - 22:55:25 \tag{4}$$

Here, t_{TEC} is the peak onset time of ionoquake is the same as defined for TEST-1 in Equation (3). The $t2_{detection}$ in Equation (4) the maximum uplift time. Figure 4(C, D) shows the results for the $t1_{detection}$ and $t2_{detection}$. One can see that within 50 to 200 km epicentral distance, both the $t1_{detection}$ and $t2_{detection}$ are less than 400 seconds.

Moreover, we note that in Equation (4), the t_{TEC} corresponds to the first peak of ionoquake, and it is subtracted from the earthquake onset time of 22:54:32. However,

in this scenario, the onset time of an ionoquake is more correct than the time of the first peak of ionoquake. This will however decrease the $t1_{\text{detection}}$. For instance, at a frequency of 4.3 mHz, the onset time of the ionoquake will occur about 116 seconds earlier than the time of the peak of the ionoquake. Therefore, in Figure 4(C, D), the appropriate ionoquake detection time will shift by -116 seconds at the frequency of 4.3 mHz. Consequently, in the vicinity of the epicenter the ionoquake detection time can be around 300 seconds, which might seem too short knowing that the "nominal" propagation of CID is about 7-10 minutes. Such a short timing could be related to low elevation angles during the detection of ionoquakes, that will lead to lower and much lower altitudes of detection, or higher vertical and horizontal propagation speeds because of transformation of acoustic waves into shock-acoustic waves due to non-linear effects. Below we discuss all these possible explanations.

4.3 Propagation speed and acoustic wave energetics

Relative to the location of the minimum detection time, the averaged propagation speed of the ionoquakes can be estimated as follows:

$$v = \frac{d - d_{\text{generation}}}{t - t_{\text{generation}}} \quad \Longrightarrow v1 = \frac{d - d_0}{t - t_0} \quad or \quad v2 = \frac{d - d_{eq}}{t - t_{eq}} \tag{5}$$

where (d, t) are the coordinates of the ionoquake in Figure 4(B), $(\mathrm{d_{generation}}, \mathrm{t_{generation}})$ are the coordinates of the ionoquake at the time of generation, (d_0, t_0) are the coordinates of the ionoquake corresponding to the minimum detection time in Figure 4(B), and (d_{eq}, t_{eq}) are the location of the epicenter and the onset time of the earthquake. The speed $v1$ sets the upper limit for the actual speed since the ionoquakes are possibly generated either at the minimum detection time or slightly earlier. The speed $v2$ sets the lower limit for the actual speed since ionoquakes are certainly generated after the onset time of earthquake t_{eq}. Therefore, the actual speed resides in between the lower $v2$ and upper $v1$ limits. Figure S3 shows the distribution of $v1$ and $v2$ as a function of ionoquake detection time and CO03-SIP distance. We note that they are in the range of 0.25-1.5 km/s such that the early detected ionoquakes have predominantly large speeds. For instance, rapid ionoquakes with a detection time of 250-400 seconds predominantly propagate faster than 0.75 km/s which is the acoustic speed range in the upper atmosphere. Previous studies have found that acoustic-gravity waves resulting from ground vibration can efficiently couple with the ionosphere and give rise to the ionoquakes (Rolland et al., 2013; Sanchez et al., 2022). If a wave responsible for coupling propagates faster than 0.75 km/s, it arrives at 180 km or higher altitude in 250-400 seconds. Therefore, the detection time and propagation speed of rapid ionoquakes suggest the altitude of detection of rapid ionoquakes to be above 180 km altitude, i.e., in the upper atmosphere where acoustic speed is faster than 0.75 km/s. Therefore, the methodology of ionoquake detection time estimation and their propagation speed estimation validate each other. Moreover, it is correct to say that the majority of rapid ionoquakes originate in the altitude range between 180 km and H_{ION}=300 km. Interestingly, simulation study by Chum et al. (2016) for the Illapel earthquake finds significant air particle disturbance in the altitude range of 170-250 km, raising the possibility of the majority of ionoquakes to be in this altitude range, as found in the present study. Also, the simulation study by Kherani et al. (2012) demonstrated the acoustic-gravity wave with a vertical phase speed of more than 600 m/s to give rise to the coseismic TEC disturbances within (300) 360 seconds at the height of 180 (250) km.

The lower limit $v2$ distribution in Figure S3 also attains the lowest of about 0.25 km/s for the early detected ionoquakes in the vicinity of the epicenter. This is due to the instantaneous generation ($\mathrm{t_{generation}} = \mathrm{t_{eq}}$) assumption in (5) which is not quite realistic. For the large earthquake of the 2011 Japan tsunami, the simulation of the Seismo-Atmosphere-Ionosphere (SAI) coupling revealed that the ionoquake can be developed within 360 seconds from the earthquake onset due to the fast-propagating Acoustic-Gravity

wave energetics (Kherani et al., 2012). Therefore, the definition $v1$ in (5) and the corresponding distribution in Figure S3(A) represent a realistic scenario. Moreover, in the present study, the ionoquake detection time of 250-400 seconds can be associated with the SAI coupling mechanism energized by the acoustic-gravity wave.

4.4 Ionoquake detection time during the Mw8.2 Iquique earthquake of 01 April, 2014

Figures 6-7 show our results for the Iquique earthquake of 01 April 2014. The temporal-spectral characteristics of V_{SISM} and TEC data in Figure 6(A1-A2) and the estimation of $t_{detection}$ in Figure 6(A3) reveal the detection of ionoquakes starting from 430 seconds after the peak onset time of V_{SISM} for the frequency range of 2 mHz-10 mHz. The conventional detection time $t1_{detection}$, represented by yellow circles in Figure 6(A3) is in between 600-700 seconds which suffers from the time shift effects, as discussed in section 4.1.1. The relationship between $t_{detection}$ and seismic-SIP distance in Figure 7 shows the two-direction propagating ionoquakes with the earliest ionoquake location near the epicenter for H_{ION}=200 km. We note the detection of several rapid ionoquakes in 400-430 seconds within 200 km seismic-SIP distance, i.e., within about 250 km epicentral distance. The detection of rapid ionoquakes in the case of the Iquique earthquake is slightly delayed, in comparison to the much earlier detection (lower than 400 seconds) in the case of the Illapel earthquake. This suggests that not all strong earthquakes produce rapid-ionoquakes detectable within 400 seconds from the peak onset time of the ground vibration.

4.5 Ionoquake detection time during the Mw7.4 Sanriku-Oki earthquake of March 9, 2011

We applied our newly developed method to seismic and TEC data around the epicentral area of the Sanriku-oki earthquake (Figures 8-9). The temporal-spectral characteristics of V_{SISM} and TEC data in Figure 8(A1-A2) and the estimation of $t_{detection}$ in Figure 8(A3) reveal the detection of ionoquakes between 240-400 seconds for the frequency range of 2.5 mHz-10 mHz. The conventional detection time $t1_{detection} = t_{TEC} - 02:45:20$, represented by yellow circles in Figure 8(A3) also below 400 seconds for frequencies below 5 mHz. Figure 9 reveals the detection of rapid ionoquakes, as close as 100 km of the epicentral distance. The relationship between the $t_{detection}$ and the seismic-SIP distance shows two-direction propagating ionoquakes from the epicentral region for H_{ION}=150 km-180 km.

Previously, Thomas et al. (2018) and Astafyeva and Shults (2019) reported the detection of the first ionoquakes at 430 seconds and 470-480 seconds respectively at the altitudes 150 km and 180-190 km, respectively. Our methodology applied for the same LOS as in Thomas et al. (2018) and Astafyeva and Shults (2019) shows quite similar results: The conventional detection time $t1_{detection}$, represented by yellow-circles in Figure S4(A3-B3) is 430-520 seconds. However, based on the $t_{detection}$, the earliest ionoquakes are detected at about 320 to 460 seconds, as shown by the gray circles in Figure S4(A3-B3). Moreover, H_{ION}=150 km-180 km of the present methodology confirms the altitude of the earliest ionoquakes reported in the previous studies of Thomas et al. (2018) and Astafyeva and Shults (2019). Therefore, our methodology estimates the true earliest arrivals of the ionoquakes/CID, in addition to the altitude of detection.

Supplementary Figure S5(A) shows the results for conventional detection time $t1_{detection}$ in the same format as Figure 9(B). For comparison, Figure 9(B) is re-drawn as Figure S5(B). The conventional method detects the earliest ionoquakes 350-400 seconds after the earthquake onset time though they are few compared to the number of earliest ionoquakes detected from the newly developed method in Figure S5(B). Therefore, both conventional and the newly developed methods detect the earliest ionoquakes in less than

400 seconds from the earthquake onset time and from the time of the peak seismic uplift.

5 Rapid Ionoquakes from Seismo-Atmosphere-Ionosphere Coupling

Past simulation studies (e.g., Kherani et al. (2012, 2016)) have found that the SAI coupling energized by the Acoustic-Gravity waves (AGWs) generates rapid ionoquakes in the upper thermosphere within 360 seconds from the earthquake onset. The rapid ionoquakes of the present study are likely to be associated with this coupling mechanism. However, the simulation study of Kherani et al. (2016) was for the case of a tsunami. For an earthquake, no simulation study is available to support the early arrival within 360 seconds from the mainshock onset of the present study. The simulation study of Chum et al. (2016) for the Illapel earthquake demonstrates the onset time of air particle disturbances only 530 seconds after the earthquake at 800 km epicentral distance. Consequently, in the vicinity of the epicenter, the disturbance should be detected several hundreds of seconds earlier.

We examine this possibility by solving the governing equations of the ground uplift-Acoustic-Gravity wave-Ionospheric disturbances coupling mechanism, presented by Kherani et al. (2012) for the Tohoku-Oki event and later employed by Sanchez et al. (2022) for the Ridgecrest earthquake. In Figures 10-11, we demonstrate the simulation results for the Illapel earthquake. We note in Figure 10 that the observed and simulated waveforms of ionoquakes are fairly good in agreement. Moreover, in Figure 11, observed and simulated ionoquake detection times are in the same time range of 260-400 seconds. Therefore, the physical mechanism responsible for the rapid ionoquakes Seismo-Atmosphere-Ionosphere coupling dynamics energized by the Acoustic-Gravity waves.

The supplementary Figure S6 demonstrates the vertical propagation of simulated acoustic-gravity waves above the epicenter. We note that from the ground uplift, numerous waves with wavefronts of different slops i.e., of different phase speeds are launched into the atmosphere. This is owing to the numerous scale heights and duct sizes present in the atmosphere, that allow numerous wavelengths at a given frequency to be sustained in the atmosphere. We note that the waves with significant amplitudes of about 10-20 m/s arrive at 160 km altitude at 22.975 hours from the mainshock onset time of 22.91 hours i.e., the waves arrive in about 240 seconds from the onset. These waves have wavelengths comparable to the size of the longest atmospheric duct of about 150 km and at the acoustic frequencies, they propagate with a phase speed of about 600 m/s or more. Therefore, in the rapid development of ionoquakes, the long wavelength AGWs participate, as also found by Kherani et al. (2012). We note in Figure S6 that the though the phase speed is about 600 m/s or more, the amplitude of the wave i.e., the fluid oscillation is about 10-20 m/s, much slower than the average atmospheric sound speed. Therefore, such a fast propagating wave is not a shock acoustic wave, the wave which is characterized by a phase speed slower than the average atmospheric sound speed and an amplitude comparable to the thermospheric sound speed (Zettergren et al., 2017).

6 Summary

We report early detections of co-seismic ionospheric disturbances (or ionoquakes) associated with the 2015 Illapel, the 2014 Iquique, and the 2011 Sanriku-Oki earthquakes. Using Total-Electron-Content (TEC) and seismic measurements, the study compares ionoquakes from our new and previous methods. The new method relies on applying the same data processing procedures to the seismic and TEC data, and on estimating the time of the peak of the seismic and TEC vibrations to obtain the ionoquake detection time. The advantage of our method is its independence from the seismological models. The method produces the expected prolongation in ionoquake detection time with increasing distance from the epicenter. Moreover, the method allows locating the earliest detected ionoquakes

which turns out to be near the epicenter. The localization is more accurate for the thin ionospheric layer centered around an altitude of 300 km for the Illapel, 200 km for the Iquique, and 150-180 km altitude for the Sanriku-Oki earthquakes. The new method also finds spectral and propagation characteristics of the earliest ionoquakes predominantly in the acoustic range. A comparative study with the conventional ionoquake detection time method highlights a new result that the detection time of earliest ionoquakes is within 400 seconds from the earthquake onset time and from the time of peak seismic uplift, for the Illapel and Sanriku-Oki earthquakes. For the Iquique earthquake, the new method detects the ionoquakes as early as 430 seconds from the time of the peak seismic uplift. Based on numerical simulation of the Seismo-Atmosphere-Ionosphere (SAI) coupling mechanism, the study associates the rapid ionoquakes with the SAI coupling energized by the acoustic-gravity waves.

Open research statement

The GNSS data for the earthquakes in Chile are available at the UNAVCO web-service (`https://www.unavco.org/data/gps-gnss/data-access-methods/gnss-data-access-notebook/gnss-data-access-notebook.html`) and CSN (`http://gps.csn.uchile.cl/`). The GNSS data for the 2011 Sanriku earthquake are available from the GeoSpatial Authority of Japan (GSI, terras.go.jp) via `http://datahouse1.gsi.go.jp/terras/terras_english.html`). The seismic data can be downloaded from the IRIS (`http://ds.iris.edu/wilber3/find_event`)

Acknowledgments

This work was supported by the joint French-Brazilian project "IONO-DIET" funded by the French National Research Agency (ANR, grant ANR-22-CE49-0011) and by the Fundação de Amparo à Pesquisa do Estado de São Paulo (FAPESP) process 2022/03502-6. We thank the Brazilian Ministry of Science, Technology and Innovation and the Brazilian Space Agency. S. A. Sanchez thanks the Coordenação de Aperfeiçoamento de Pessoal de Nível Superior (CAPES) and FAPESP processes 88887.351785/2019-00 and 2023/07807-9 respectively. E. A. Kherani thanks the financial support of the Conselho Nacional de Desenvolvimento Científico e Tecnológico (CNPq) through grant 307496/2015-5. E. Astafyeva thanks the financial support of the French Space Agency (CNES), project "RealDetect". E. R. de Paula thanks CNPq 202531/2019-0 and INCT GNSS-NavAer Project under grants CNPq 465648/2014-2 and FAPESP 2017/50115-0.

References

Afraimovich, E. L., Astafyeva, E. I., Demyanov, V. V., Edemskiy, I. K., Gavrilyuk, N. S., Ishin, A. B., ... Zhivetiev, I. V. (2013). A review of GPS/GLONASS studies of the ionospheric response to natural and anthropogenic processes and phenomena. *Journal of Space Weather and Space Climate*, *3*, A27. doi: org/10.1051/swsc/2013049

Astafyeva, E. (2019). Ionospheric detection of natural hazards. *Reviews of Geophysics*, *57*, 1265–1288. doi: s10.1029/2019RG000668

Astafyeva, E. (2020). Detecting Earth's natural hazards high up in the sky. *EOS*, *101*. doi: 10.1029/2020EO145982

Astafyeva, E., Heki, K., Kiryushkin, V., Afraimovich, E., & Shalimov, S. (2009). Two-mode long-distance propagation of coseismic ionosphere disturbances. *Journal of Geophysical Research: Space Physics*, *114*(A10). doi: org/10.1029/2008JA013853

Astafyeva, E., Lognonné, P., & Rolland, L. M. (2011). First ionosphere images for the seismic slip on the example of the Tohoku-oki earthquake. *Geophys. Res. Letters*, *38*, L22104. doi: 10.1029/2011GL049623

Astafyeva, E., Rolland, L. M., Lognonné, P., Khelfi, K., & Yahagi, T. (2013). Parameters of seismic source as deduced from 1Hz ionospheric GPS data: case-study of the 2011 Tohoku-oki event. *Journal of Geophys. Research*, *118*, 5942–5950. doi: 10.1002/jgra50556

Astafyeva, E., Rolland, L. M., & Sladen, A. (2014). Strike-slip earthquakes can also be detected in the ionosphere. *Earth and Planetary Science Letters*, *405*, 180–193. doi: org/10.1016/j.epsl.2014.08.024

Astafyeva, E., & Shults, K. (2019). Ionospheric GNSS imagery of seismic source: Possibilities, difficulties, and challenges. *Journal of Geophysical Research: Space Physics*, *124*(1), 534–543. doi: org/10.1029/2018JA026107

Bagiya, M. S., Sunil, A., Rolland, L., Nayak, S., Ponraj, M., Thomas, D., & Ramesh, D. S. (2019). Mapping the impact of non-tectonic forcing mechanisms on GNSS measured coseismic ionospheric perturbations. *Scientific Reports*, *9*(1), 18640. doi: org/10.1038/s41598-019-54354-0

Bagiya, M. S., Thomas, D., Astafyeva, E., Bletery, Q., Lognonné, P., & Ramesh, D. S. (2020). The ionospheric view of the 2011 Tohoku-Oki earthquake seismic source: the first 60 seconds of the rupture. *Scientific reports*, *10:5232*. doi: 10.1038/s41598-020-61749-x

Bravo, M., Benavente, R., Foppiano, A., Urra, B., & Ovalle, E. (2022). Traveling ionospheric disturbances observed over south america after lithospheric events: 2010–2020. *Journal of Geophysical Research: Space Physics*, *127*(4), e2021JA030060. doi: org/10.1029/2021JA030060

Cahyadi, M. N., & Heki, K. (2015). Coseismic ionospheric disturbance of the large strike-slip earthquakes in North Sumatra in 2012: Mw dependence of the disturbance amplitudes. *Geophysical journal international*, *200*(1), 116–129. doi: org/10.1093/gji/ggu343

Calais, E., & Minster, J. B. (1995). GPS detection of ionospheric perturbations following the January 17, 1994, Northridge earthquake. *Geophysical Research Letters*, *22*(9), 1045-1048. doi: org/10.1029/95GL00168

Chum, J., Cabrera, M. A., Mošna, Z., Fagre, M., Baše, J., & Fišer, J. (2016). Nonlinear acoustic waves in the viscous thermosphere and ionosphere above earthquake. *Journal of Geophysical Research: Space Physics*, *121*(12), 12,126-12,137. doi: org/10.1002/2016JA023450

Chum, J., Hruska, F., Zednik, J., & Lastovicka, J. (2012). Ionospheric disturbances (infrasound waves) over the Czech Republic excited by the 2011 Tohoku earthquake. *Journal of Geophysical Research: Space Physics*, *117*(A8). doi: org/10.1029/2012JA017767

Coster, A., Williams, J., Weatherwax, A., Rideout, W., & Herne, D. (2013). Accuracy of GPS total electron content: GPS receiver bias temperature dependence. *Radio Science*, *48*(2), 190-196. doi: doi.org/10.1002/rds.20011

Heki, K., & Ping, J. (2005). Directivity and apparent velocity of the coseismic ionospheric disturbances observed with a dense GPS array. *Earth and Planetary Science Letters*, *236*(3-4), 845–855. doi: org/10.1016/j.epsl.2005.06.010

Hofmann-Wellenhof, B., Lichtenegger, H., & Wasle, E. (2008). *GNSS - Global Navigation Satellite Systems*. Springer-Verlag Vienna. doi: org/10.1007/978-3-211-73017-1

Hosseini, K., & Sigloch, K. (2017). ObspyDMT: a Python toolbox for retrieving and processing large seismological data sets. *Solid Earth*, *8*(5), 1047–1070. doi: 10.5194/se-8-1047-2017

Kherani, E. A., Lognonné, P., Hébert, H., Rolland, L., Astafyeva, E., Occhipinti, G., ... de Paula, E. R. (2012). Modelling of the total electronic content and magnetic field anomalies generated by the 2011 Tohoku-Oki tsunami and associated acoustic-gravity waves. *Geophysical Journal International*, *191*(3), 1049-1066. doi: org/10.1111/j.1365-246X.2012.05617.x

Kherani, E. A., Rolland, L., Lognonné, P., Sladen, A., Klausner, V., & de Paula,

E. (2016). Traveling ionospheric disturbances propagating ahead of the Tohoku-Oki tsunami: a case study. *Geophysical Journal International*, *204*(2), 1148–1158. doi: doi.org/10.1093/gji/ggv500

Klobuchar, J. A. (1987). Ionospheric time-delay algorithm for single-frequency GPS users. *IEEE Transactions on aerospace and electronic systems*(3), 325–331. doi: 10.1109/TAES.1987.310829

Liu, J., Tsai, Y., Chen, S., Lee, C., Chen, Y., Yen, H., ... Liu, C. (2006). Giant ionospheric disturbances excited by the M9.3 Sumatra earthquake of 26 December 2004. *Geophysical Research Letters*, *33*(2). doi: org/10.1029/2005GL023963

Lognonné, P. (2009). Seismic waves from atmospheric sources and atmospheric/ionospheric signatures of seismic waves. In *Infrasound monitoring for atmospheric studies* (pp. 281–304). Springer. doi: org/10.1007/978-1-4020-9508-5_10

Manta, F., Occhipinti, G., Feng, L., & Hill, E. M. (2020). Rapid identification of tsunamigenic earthquakes using GNSS ionospheric sounding. *Scientific Reports*, *10*(1), 11054. doi: org/10.1038/s41598-020-68097-w

Occhipinti, G. (2015). The seismology of the planet mongo: The 2015 ionospheric seismology review. *AGU Books, Subduction Dynamics: From Mantle to Mega Disasters, Editors: G. Morra, D. A. Yuen, S. King, S. M. Lee, S. Stein*. doi: 10.1002/9781118888865.ch9

Occhipinti, G., Rolland, L., Lognonné, P., & Watada, S. (2013). From Sumatra 2004 to Tohoku-Oki 2011: The systematic GPS detection of the ionospheric signature induced by tsunamigenic earthquakes. *Journal of Geophysical Research: Space Physics*, *118*(6), 3626–3636. doi: org/10.1002/jgra.50322

Rolland, L. M., Lognonné, P., & Munekane, H. (2011). Detection and modeling of rayleigh wave induced patterns in the ionosphere. *Journal of Geophysical Research: Space Physics*, *116*(A5). doi: org/10.1029/2010JA016060

Rolland, L. M., Vergnolle, M., Nocquet, J.-M., Sladen, A., Dessa, J.-X., Tavakoli, F., ... Cappa, F. (2013). Discriminating the tectonic and non-tectonic contributions in the ionospheric signature of the 2011, Mw7. 1, dip-slip Van earthquake, Eastern Turkey. *Geophysical Research Letters*, *40*(11), 2518–2522. doi: doi.org/10.1002/grl.50544

Sanchez, S. A., Kherani, E. A., Astafyeva, E., & de Paula, E. R. (2022). Ionospheric disturbances observed following the Ridgecrest earthquake of 4 july 2019 in California, USA. *Remote Sensing*, *14*(1), 188. doi: org/10.3390/rs14010188

Thomas, D., Bagiya, M. S., Sunil, P. S., Rolland, L., Sunil, A. S., Mikesell, T. D., ... Ramesh, D. S. (2018). Revelation of early detection of co-seismic ionospheric perturbations in GPS-TEC from realistic modelling approach: Case study. *Scientific reports*, *8*(1), 1–10. doi: org/10.1038/s41598-018-30476-9

Zettergren, M. D., Snively, J. B., Komjathy, A., & Verkhoglyadova, O. P. (2017). Nonlinear ionospheric responses to large-amplitude infrasonic-acoustic waves generated by undersea earthquakes. *Journal of Geophysical Research: Space Physics*, *122*(2), 2272-2291. doi: org/10.1002/2016JA023159

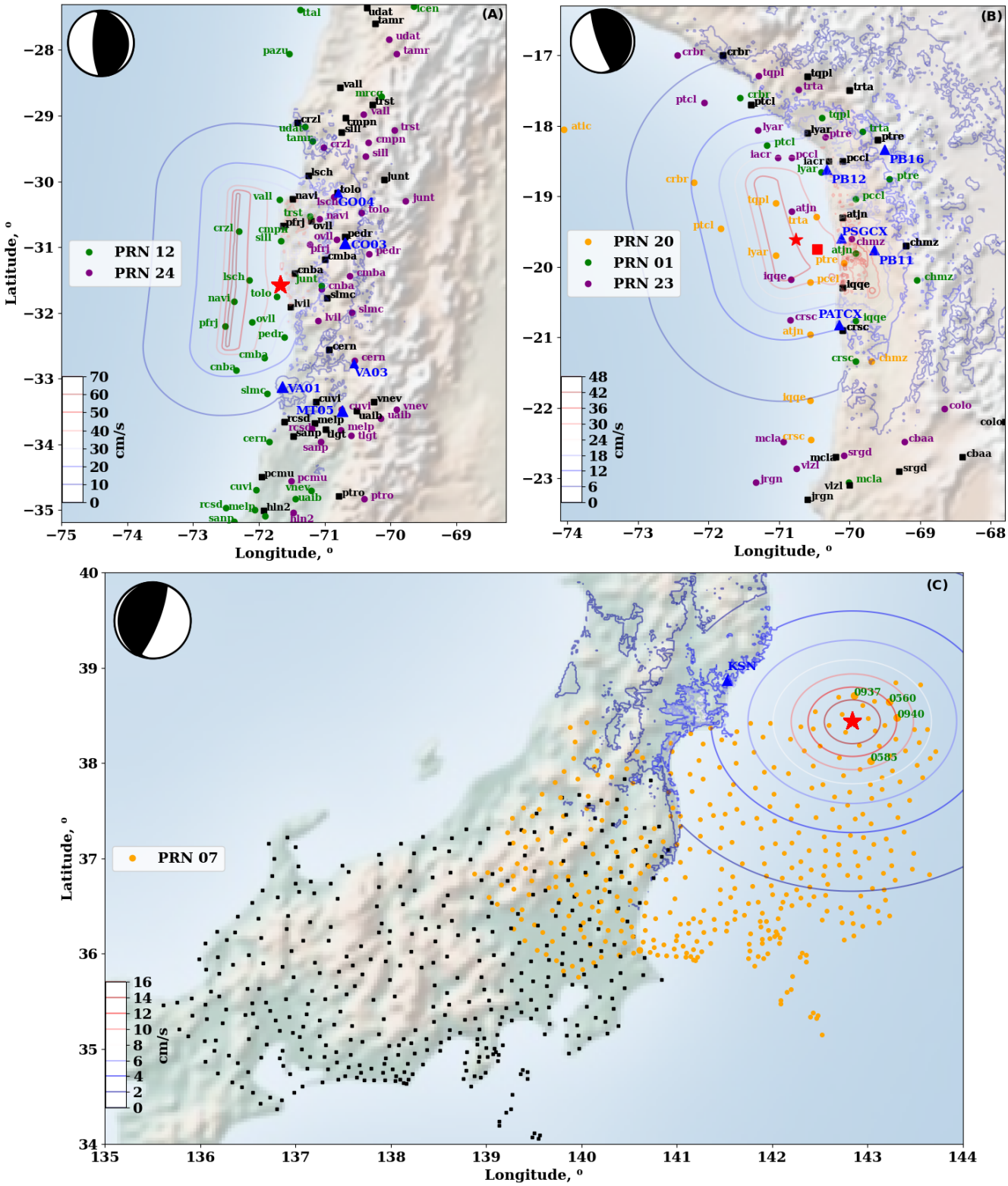

Figure 1. Locations of the 2015 Illapel (A), the 2014 Iquique (B) and the 2011 Sanriku-oki (C) earthquakes. The epicenter of the earthquakes is represented by a red star and the blue triangles show the location of the seismic stations used in this study. The dots of different colors represent the SIPs at the time when the ionoquake occurred, each color corresponds to a particular PRN. The black squares depict the location of the GNSS stations. The colored contours represent the PGVs (Peak-Ground-Velocity) for each of the earthquakes. Beach ball shows the Global Centroid Moment Tensor

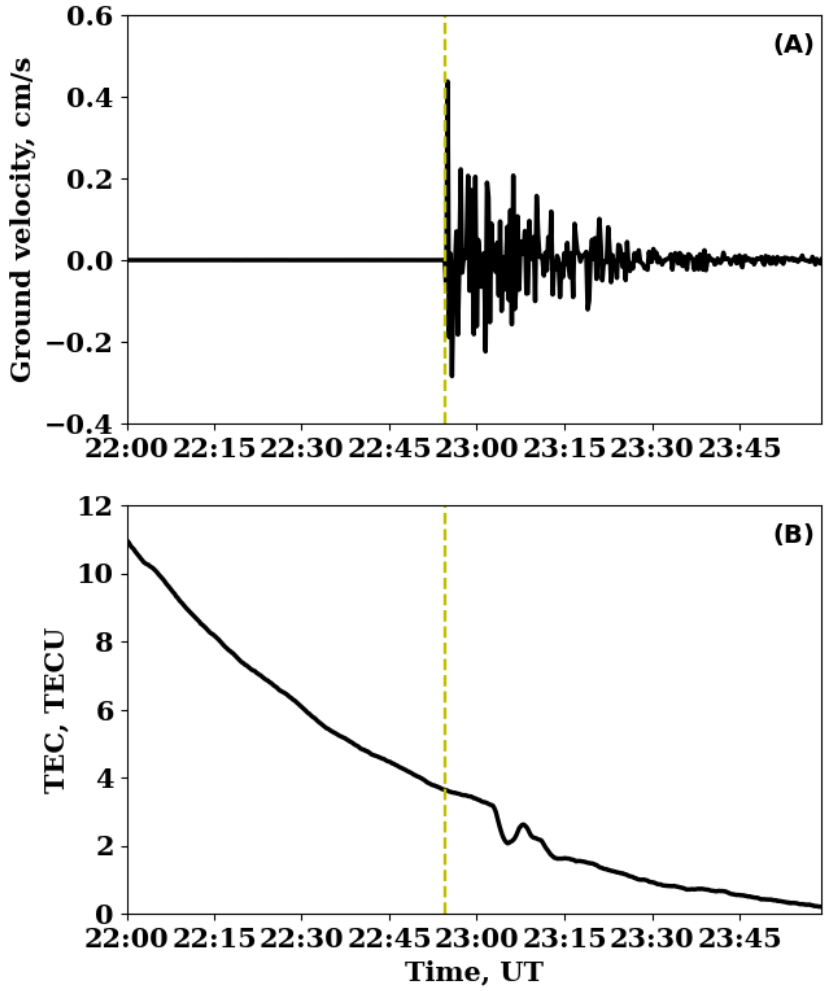

Figure 2. The 2015 Illapel earthquake: Vertical ground velocity recorded by seismic station CO03 (A), TEC time series recorded by the GNSS satellite PRN G12 and the LSCH ground receiver (B). Both the V_{SISM} and TEC time series have a resolution of 15 seconds.

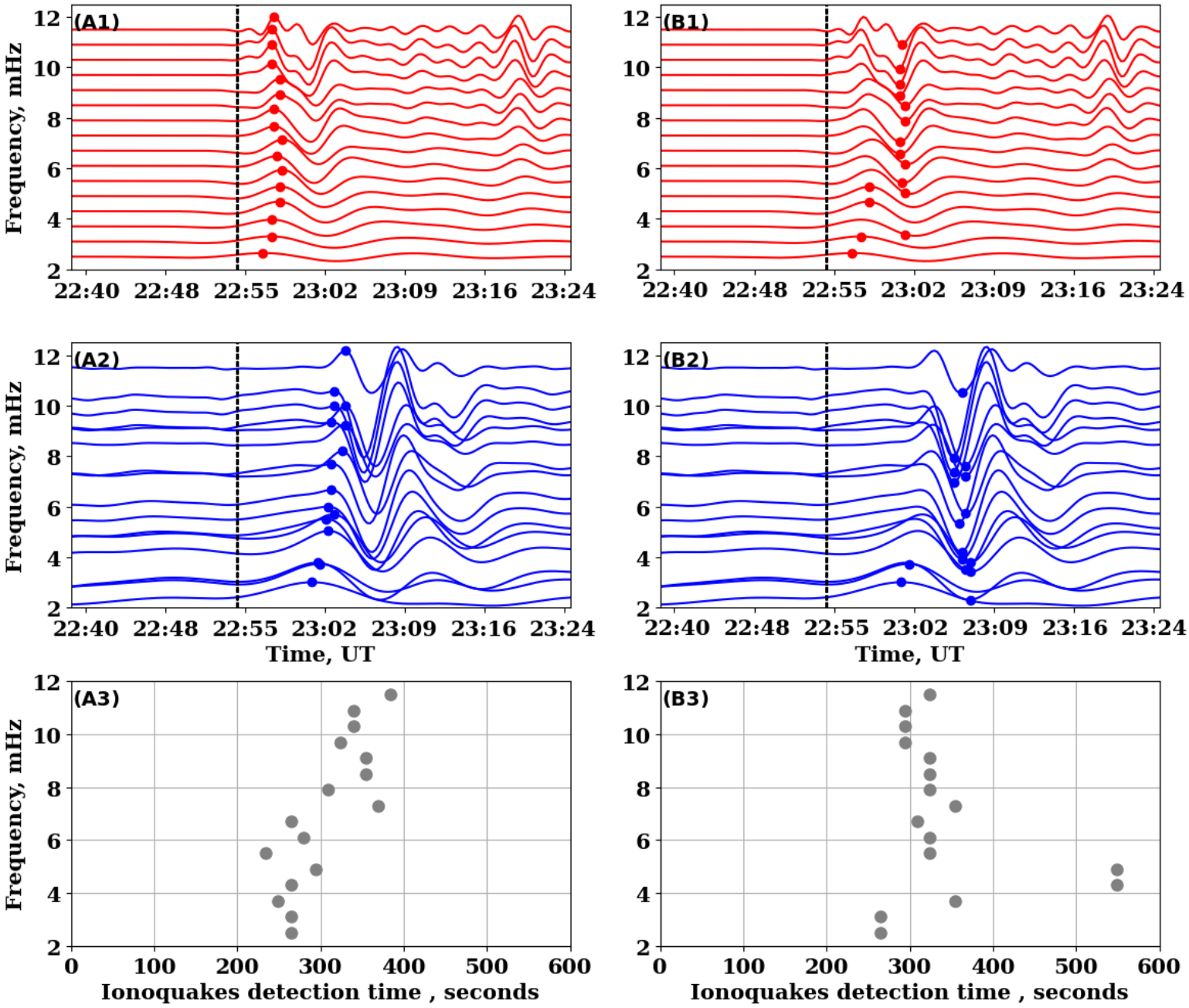

Figure 3. The 2015 Illapel earthquake: Results of TEST-1 (left) and TEST-2 (right). Panels A1-B1 show the V_{SISM} time series recorded by the CO03 seismic station for different frequencies. Panels A2 and B2 show the ΔTEC time series obtained at different frequencies for the LSCH PRN G12 station. The filled circles in (A1,A2) represent the time of the peak in the first seismic oscillation and the first ΔTEC oscillation, respectively. The filled circles in (B1, B2) show the peak in the entire series of seismic and ΔTEC oscillations, respectively. The filled circles in panels (A3, B3) represent the detection time of ionoquakes, $t_{detection}$, derived from the definition (3).

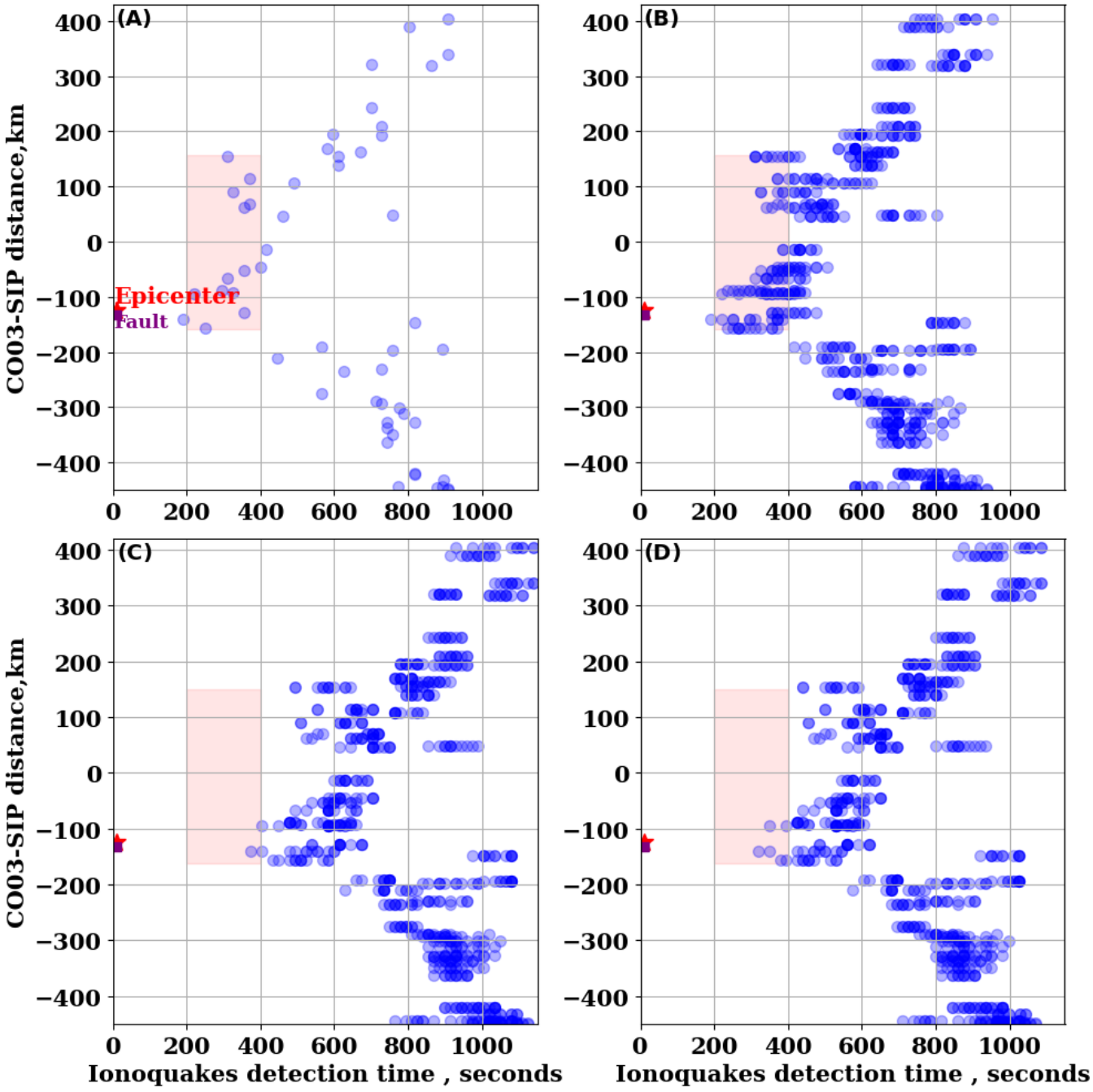

Figure 4. The 2015 Illapel earthquake: Ionoquake detection time vs. distance diagram where distance is in between seismic station (C003) and Sub-Ionospheric-Point (SIP) of Line-of-sight (LOS) of LSCH-G12 pair. Panels (A-B) correspond to the new definition $t_{detection}$ in (3) for a frequency of 3.7 mHz, and a frequency range 3.2-10 mHz, respectively. Panels (C-D) correspond to the conventional definitions $t1_{detection}$ and $t2_{detection}$ in (4), respectively for a frequency range 3.2-10 mHz. The distance of 0 km indicates the location of the CO03 seismic station. In (A-B), $t_{detection} = 0$ in the x-axis corresponds to the time of peak seismic uplift at each corresponding frequency. In (C-D), $t1_{detection} = 0$ in the x-axis corresponds to the time of earthquake onset.

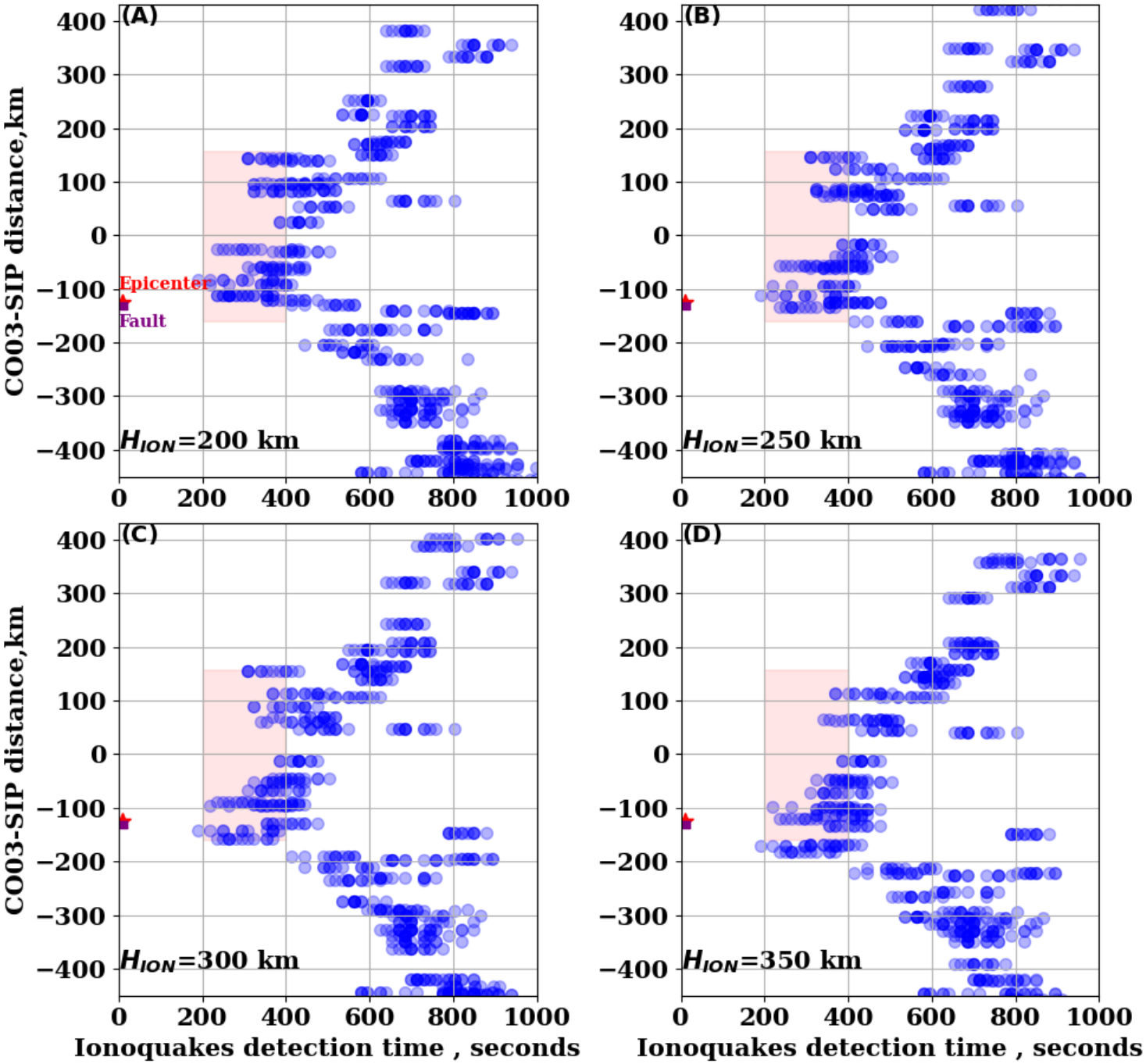

Figure 5. The 2015 Illapel earthquake: $t_{detection}$- distance diagram where distance is in between the seismic station (C003) and SIPs of LOSs of numerous GPS receiver-satellite pairs. The frequency range is 3.2-10 mHz. Four panels correspond to four values of altitude of detection (H_{ION}). The distance of 0 km indicates the location of the CO03 seismic station. $t_{detection} = 0$ in the x-axis corresponds to the time of peak seismic uplift at each corresponding frequency.

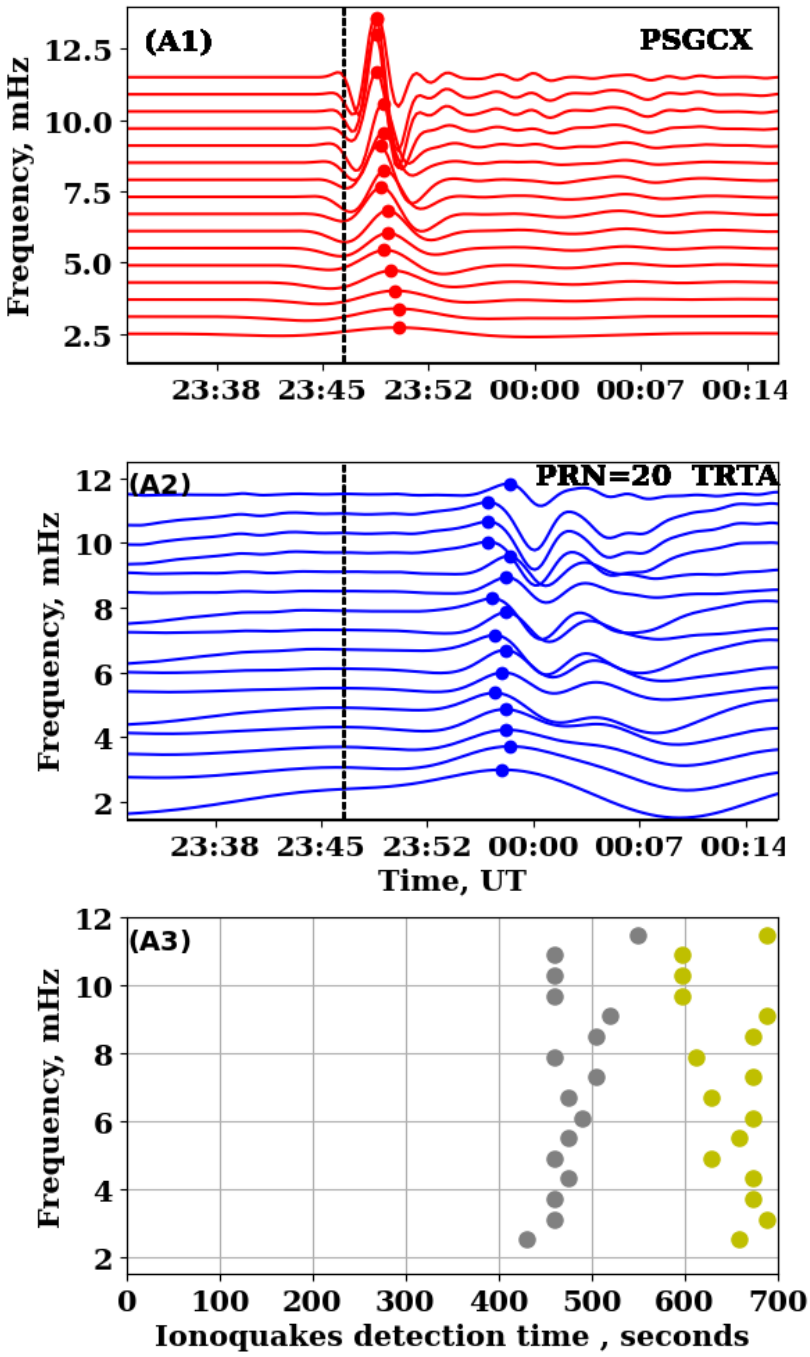

Figure 6. The 2014 Iquique earthquake with TEST-1. Panel A1 shows the V_{SISM} time series recorded by the PSGCX seismic station for different frequencies. Panel A2 shows the ΔTEC time series obtained at different frequencies for the TRTA PRN G20 station. In (A1-A2), the filled circles represent the time of the peak in the first seismic oscillation and the first ΔTEC oscillation, respectively. In panel A3, filled circles in grey and yellow correspond to the new definition, $t_{detection}$ in (3), and the conventional definition, $t1_{detection} = t_{TEC} - 23:46:47$, respectively.

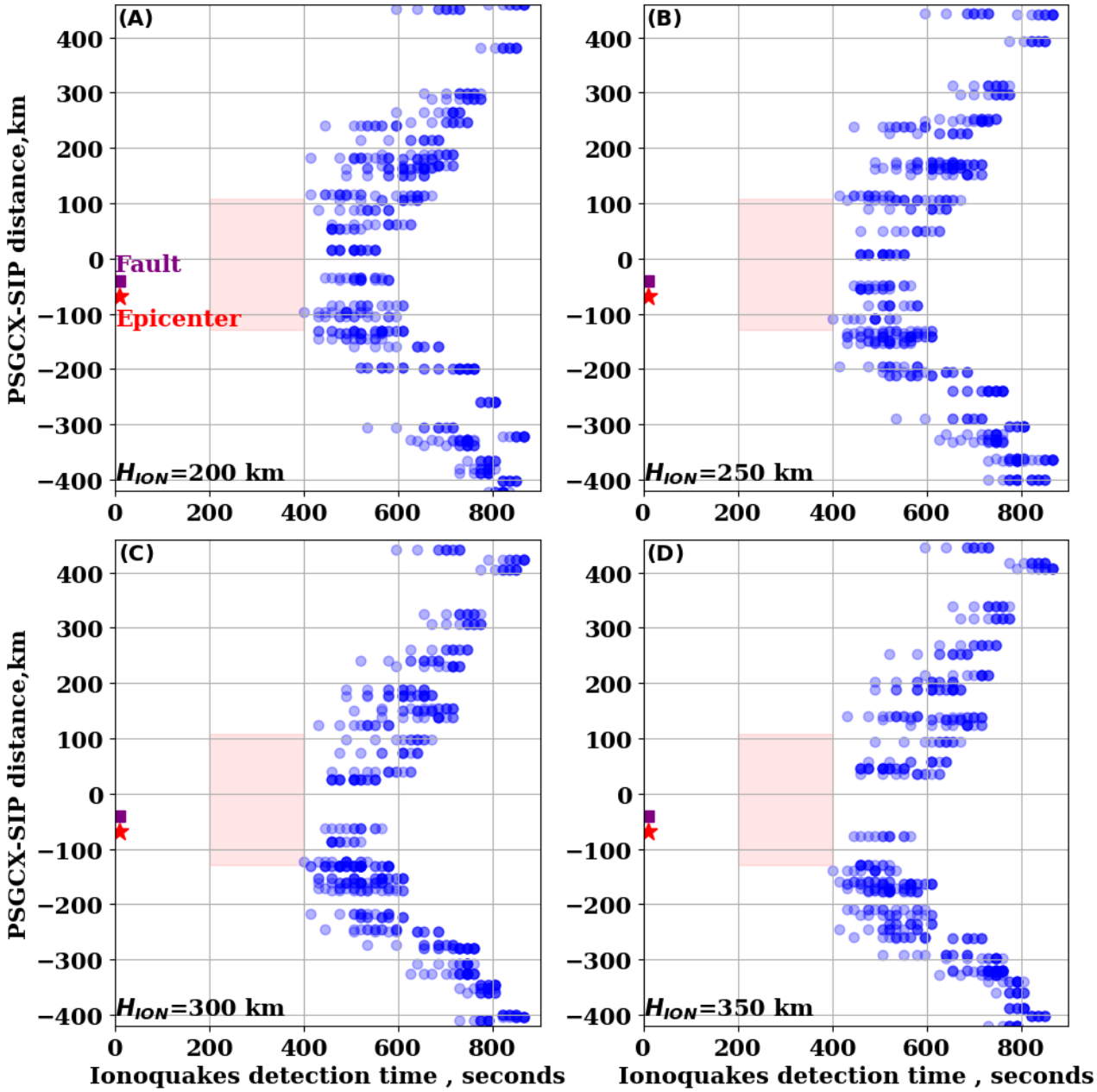

Figure 7. The 2014 Iquique earthquake: $t_{detection}$- distance diagram where distance is in between the seismic station (PSGCX) and SIPs of LOSs of numerous GPS receiver-satellite pairs. The frequency range is 3.2-10 mHz. Four panels correspond to four values of altitude of detection (H_{ION}). The distance of 0 km indicates the location of the PSGCX seismic station. $t_{detection} = 0$ in the x-axis corresponds to the time of peak seismic uplift at each corresponding frequency.

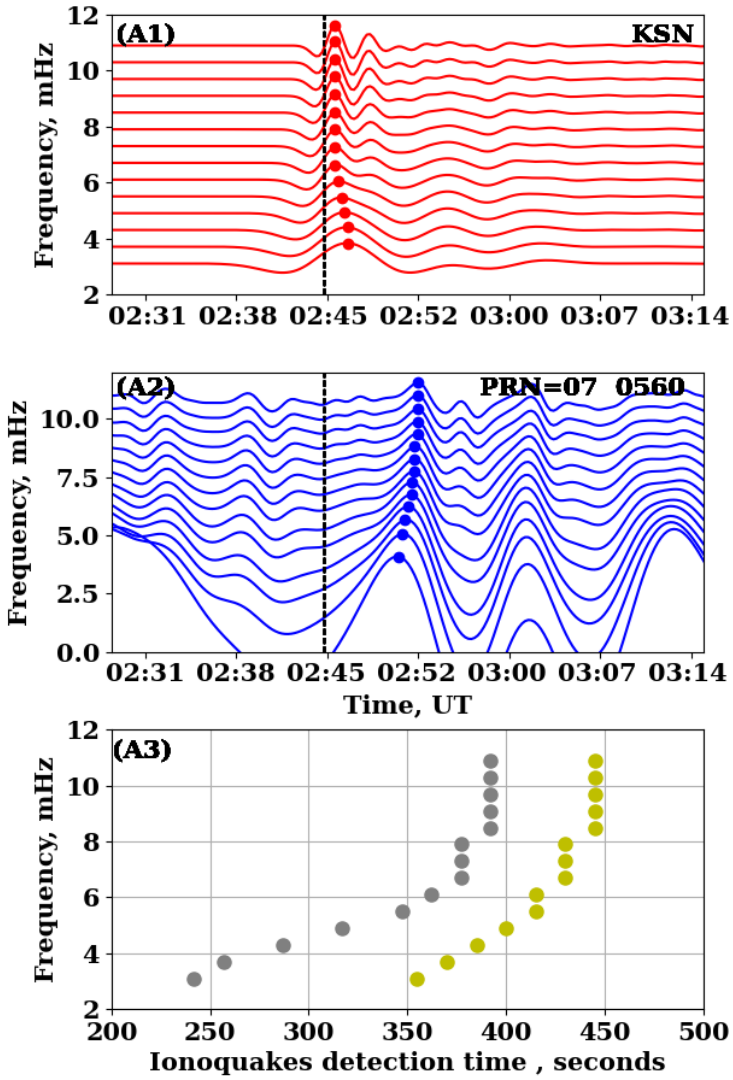

Figure 8. The 2011 Sanriku-Oki earthquake with TEST-1. Panel A1 shows the V_{SISM} time series recorded by the KSN seismic station for different frequencies. Panel A2 shows the ΔTEC time series obtained at different frequencies for the 0560 PRN G07 station. In (A1-A2), the filled circles represent the time of the peak in the first seismic oscillation and the first ΔTEC oscillation, respectively. In panel A3, filled circles in grey and yellow correspond to the new definition, $t_{detection}$ in (3), and the conventional definition, $t1_{detection} = t_{TEC} - 02:45:20$, respectively.

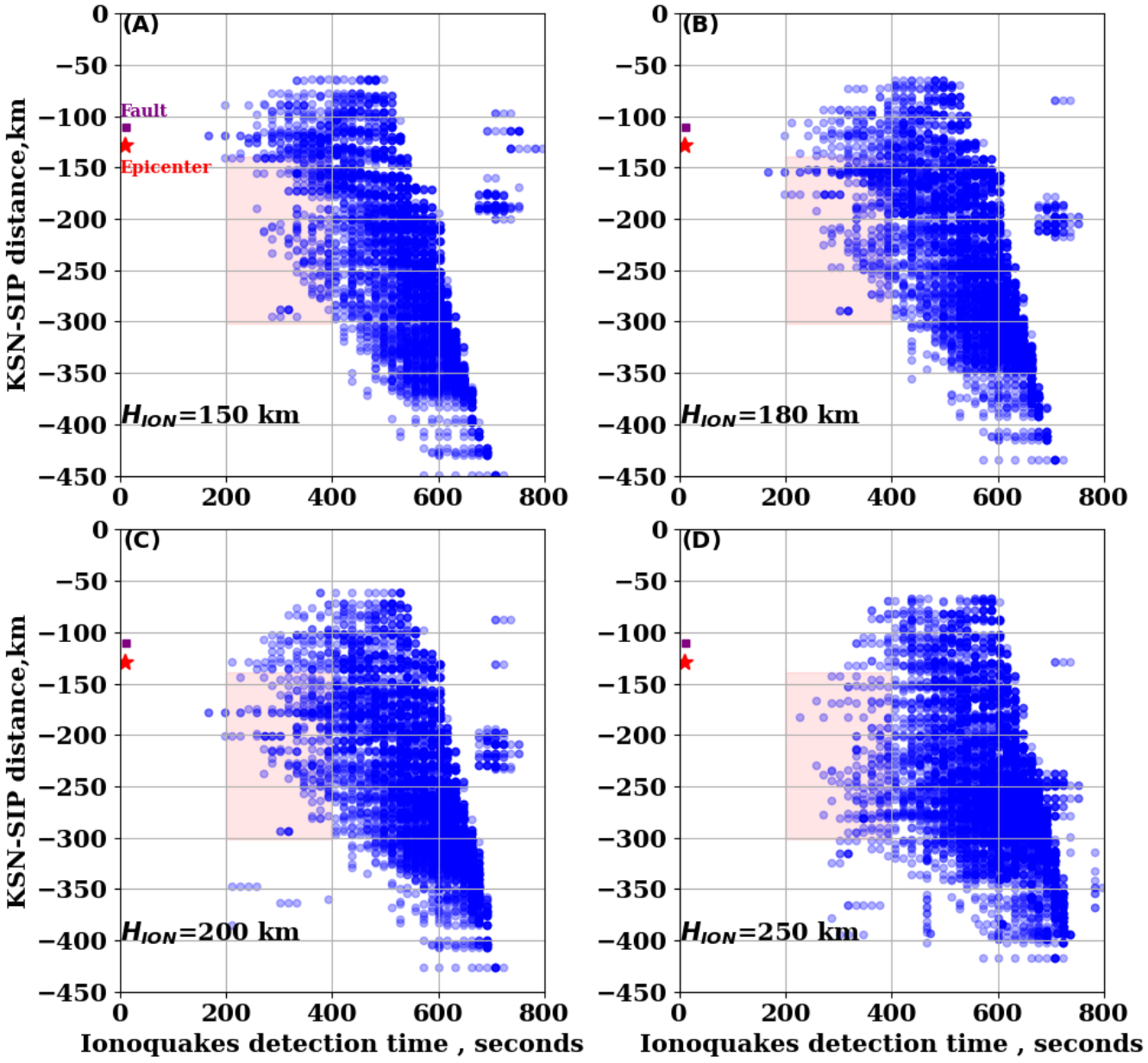

Figure 9. The 2011 Sanriku-Oki earthquake: $t_{detection}$- distance diagram where distance is in between the seismic station (KSN) and SIPs of LOSs of numerous GPS receiver-satellite pairs. The frequency range is 3.2-10 mHz. Four panels correspond to four values of altitude of detection (H_{ION}). The distance of 0 km indicates the location of the KSN seismic station. $t_{detection} = 0$ in the x-axis corresponds to the time of peak seismic uplift at each corresponding frequency.

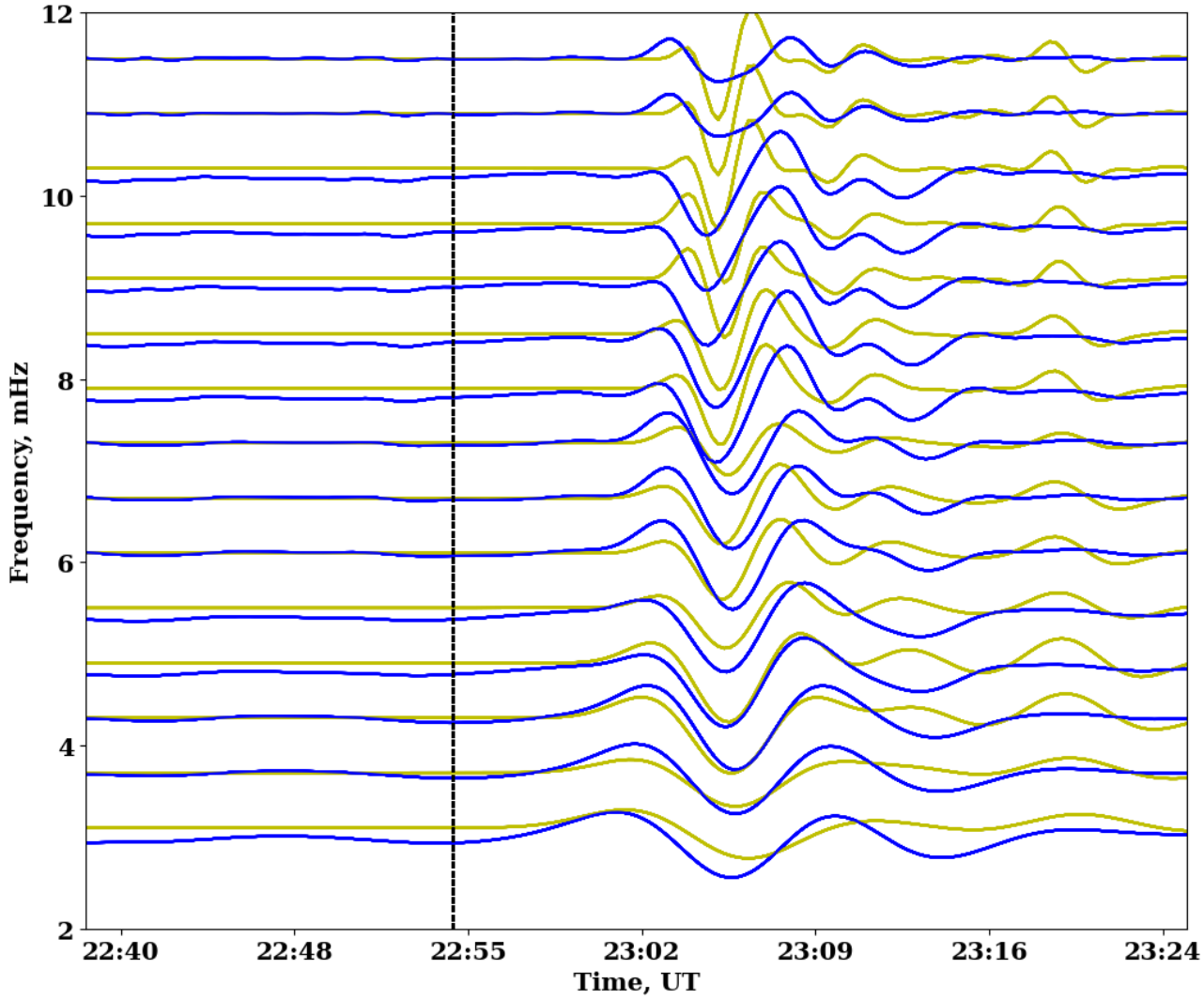

Figure 10. ΔTEC comparison between observation (blue) and simulation (yellow), for the Illapel earthquake.

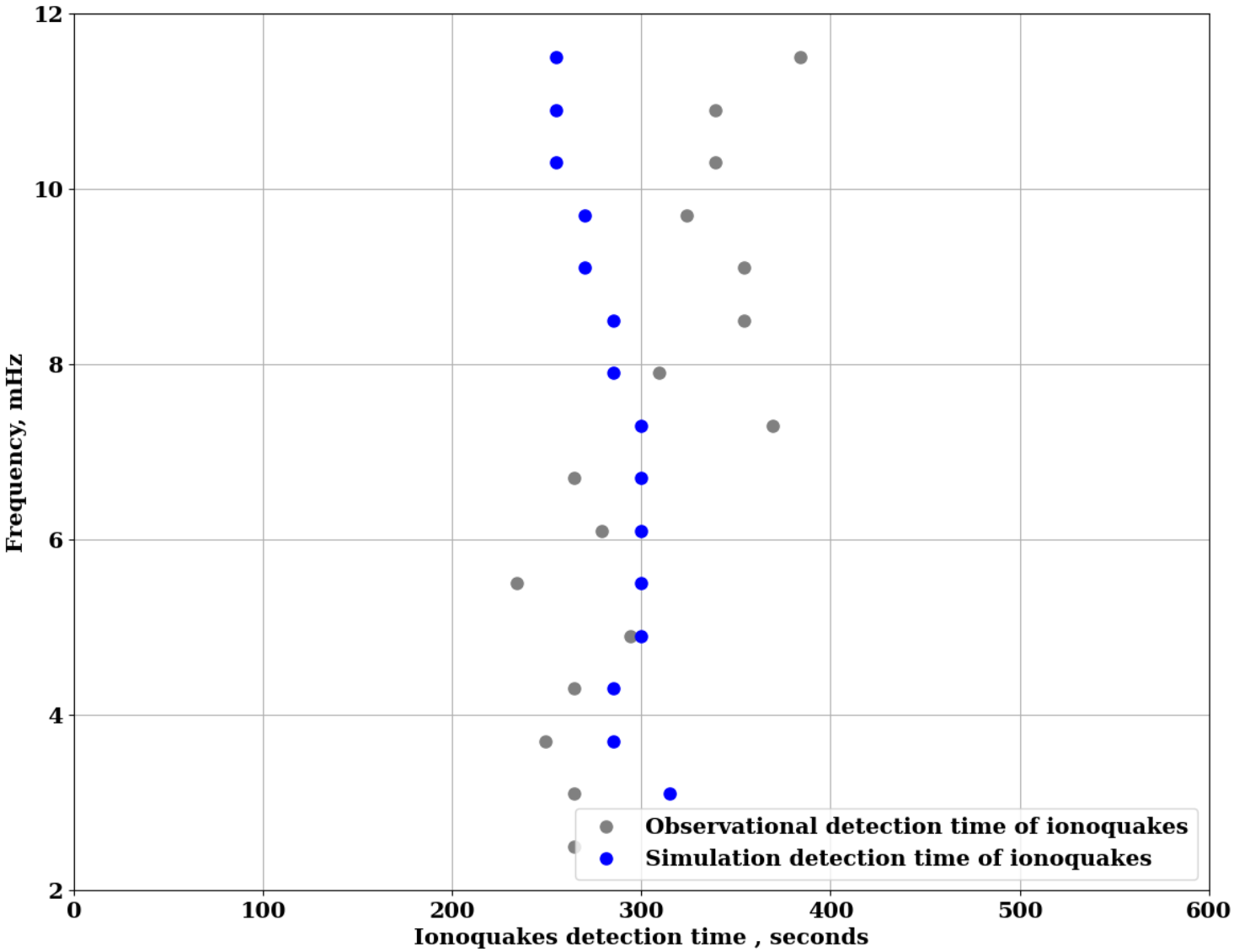

Figure 11. The 2015 Illapel earthquake. Comparison of Ionoquakes detection time between simulation and observation.